Applied Catalysis B: Environmental 303 (2022) 120907

Contents lists available at ScienceDirect

Applied Catalysis B: Environmental

journal homepage: www.elsevier.com/locate/apcatb

Integrated direct air capture and oxidative dehydrogenation of propane with CO_2 at isothermal conditions

Shane Lawson [a], Khaled Baamran [a], Kyle Newport [a], Turki Alghamadi [a], Gary Jacobs [b], Fateme Rezaei [a,*], Ali A. Rownaghi [a,*]

[a] Department of Chemical & Biochemical Engineering, Missouri University of Science and Technology, Rolla, MO 65409–1230, United States
[b] Department of Biomedical Engineering and Chemical Engineering/Department of Mechanical Engineering, The University of Texas at San Antonio, San Antonio, TX 78249–0669, United States

ARTICLE INFO

Keywords:
Dual-functional adsorbent-catalyst materials
3D printing
Direct CO_2 capture-utilization
oxidative propane dehydrogenation

ABSTRACT

Developing routes of utilizing CO_2 emissions is important for long-term environmental preservation, as storing such emissions underground will eventually become unsustainable. One way of utilizing CO_2 emissions is as a light-oxidant feedstock for oxidative dehydrogenation of propane (ODHP) to propylene. However, the adsorption and reaction steps typically occur at widely different temperatures, meaning that the thermal gradients – and by extension process energy requirements – are often unreasonably high. In recent years, dual-functional materials (DFMs) – i.e., materials comprised of a high temperature adsorbent phase alongside a heterogeneous catalyst – have been employed for combined CO_2 adsorption and utilization over one material within a single bed using a reduced thermal gradient. However, these materials have never been formed into practical contactors and have never been applied to ODHP applications. Therefore, in this study we manufactured the first-generation of DFM adsorbent/catalyst monoliths, comprised of CaO (adsorbent) and M@ZSM-5 (M = V-, Ga-, Ti-, or Ni-oxide) heterogeneous catalysts, using our novel direct metal-oxide 3D printing technique. The monoliths were vigorously characterized using N_2 physisorption, C_3H_8-DRIFTS, NH_3-TPD, Py-FTIR, H_2-TPR, XRD, XPS, and elemental mapping and were assessed for CO_2 capture/ODHP utilization at 600–700 °C. The adsorption/catalysis experiments revealed that these materials can perform both processes effectively at 600 °C, with reduced propylene yield at higher temperature, which eliminated the need for a thermal gradient between the adsorption and catalysis steps. Between the various samples, the Ti-doped monolith generated the best balance of CO_2 conversion (76%) and propylene selectivity (39%), due to the high dispersion of TiO_2, favorable redox properties and controlled acidity of the dopant. However, it was also found that varying the metal dopant could be used to control the heuristics of CO_2/C_3H_8 conversion, C_3H_6 selectivity, and C_3H_6 yield, meaning that the manufacturing process outlined herein represents a promising way of tuning the chemical properties of structured DFM adsorbent/catalyst materials. More importantly, this study establishes a promising proof-of-concept for 3D printing as a facile means of structuring these exciting composite materials and expands DFMs to the previously unexplored application of ODHP.

1. Introduction

It is a well-established and inarguable fact that the increasing atmospheric CO_2 levels are directly tied to climate change, so finding new strategies of carbon management has been at the forefront of cutting-edge scientific research over the past few decades. [1–3] One such strategy has been to implement adsorption technology, whereby CO_2 is compressed in a porous material (physisorption) or tethered to a chemically active material (chemisorption), as these techniques allow for reduced energy consumption compared to cryogenic fracturing as well as lower environmental waste compared to amine scrubbing. [4,5] Nevertheless, one difficulty of managing CO_2 in this way is how best to deal with the sequestered gaseous emissions, as this area of research remains underdeveloped. Most simply, CO_2 is usually bound to a group-II metal-oxide to form a solid carbonate, where it can then be buried underground for long term storage. As might be imagined,

* Corresponding author.
E-mail addresses: rezaeif@mst.edu (F. Rezaei), rownaghia@mst.edu (A.A. Rownaghi).

https://doi.org/10.1016/j.apcatb.2021.120907
Received 7 September 2021; Received in revised form 29 October 2021; Accepted 4 November 2021
Available online 9 November 2021

however, this approach is unattractive from an industrial standpoint because it requires a constant feedstock of metal-oxide precursor and does not incur any return on investment. Granted, the CO_2 can also be compressed and sold for commercial consumption; however, this process will inevitably lead to re-release of CO_2 into the environment elsewhere, so it cannot be considered a viable way of managing CO_2 emissions long-term. Hence, new strategies of dealing with CO_2 are necessary to preserve the global environment for future generations.

In recent years, one exciting and novel pathway of utilizing CO_2 has been to employ it as a light oxidant feedstock in paraffin dehydrogenation reactions, such as propane dehydrogenation into propylene, as this approach allows the gas to be converted into more marketable CO whilst generating valuable polymer precursors. [6–9] To this end, heterogeneous catalyst materials – such as ZSM-5 with various metal-oxide dopants – are usually employed because the zeolite phase allows for active hydrogen removal from propane, whereas the metal dopants facilitate bond formation by switching between active sites by way of valance electron oxidation with CO_2. In this way, oxidative dehydrogenation of propane (ODHP) over bifunctional heterogeneous catalysts can be considered an effective pathway of utilizing CO_2 emissions. Nevertheless, the CO_2 adsorption and subsequent ODHP reaction steps generally occur in separate beds, which drives up process energy costs because this distinction necessitates heating and cooling two systems thereby yielding large thermal gradients and long cycle times. [10] In this way, combining these two-bed adsorption/catalytic processes into a singular system can be considered an attractive notion from a process energy perspective.

Granted, performing single-bed CO_2 capture and utilization is not a straightforward or easy task, as it necessitates considerable efforts regarding the development of materials for such processes. [11–13] The reason being that the composite dual-functional material (DFM) must show a high affinity towards CO_2 at elevated temperatures and must also contain the proper acidity, redox properties, and active site density to facilitate the ODHP reaction. In our earlier work, we demonstrated the first iteration of such materials when we formulated dual-salt (K-Ca)/ZSM-5 composites with Cr_2O_3 dopants and employed them in combined CO_2 capture and utilization in oxidative dehydrogenation of ethane (ODHE) to ethylene. [10] While this study was a fundamental breakthrough in the area of DFMs, it is yet unknown if such composites can be expanded for dehydrogenation of heavier hydrocarbons, which is considerably more complicated because C_{3+} hydrocarbons are more prone to thermal cracking at the temperatures required to desorb CO_2 from the CaO adsorbent phase (i.e., 700 °C). Besides, another issue for current DFMs is that there has not yet been a report which successfully formulates these composites into structured contactors, which is a key aspect in their eventual scale-up. Regarding this issue, it is difficult to apply traditional manufacturing methods – such as pelletization, extrusion, or granulation – to dual-salt composites, since these techniques typically use water to facilitate intraparticle binding. [5] The application of water to initiate binding of these materials is problematich because the K_2O and CaO phases in the dual-salt are of high solubility and can react with water to form $Ca(OH)_2$, which will inevitably lead to unpredictable degrees of deactivation for the adsorbent material. Hence, new techniques are required to scale-up DFM materials.

One possible approach through which to structure these materials would be to employ the direct 3D printing technique which we reported in a recent series of studies to formulate insoluble metal oxides into customizable heterogeneous catalysts. [14–17] Not only does this approach allow for unprecedentedly high metal loading and exceptional freedom in dopant incorporation, but it also has repeatedly generated heterogeneous catalysts with outstanding reactivity performance independent of the reaction itself. For example, the catalysts have all achieved unheard of conversions, desired-product selectivities, and zero deactivations in ODHP, n-hexane cracking, and methanol/dimethyl ether reactions, thus cementing the potential of the direct printing technique as a means of structured catalyst manufacturing. In efforts to apply this approach for the scale-up of DFM composites, we theorized that $CaCO_3$ could be used in the printing inks, as this material is both insoluble and can be calcined to generate the CaO adsorbent phase. To this end, we postulated that this technique could be used to generate the first-ever structured DFM adsorbent/catalyst materials.

Motivated by this possibility, we embarked on a study which directly formulates 3D-printed DFM CaO/ZSM-5 monoliths with V-, Ni-, Ti-, and Ga-oxide dopants for use in single bed CO_2 capture and utilization in ODHP. The monoliths were first vigorously characterized using various techniques including: X-ray diffraction (XRD), X-ray photoelectron spectroscopy (XPS), N_2 physisorption, NH_3-temperature programmed desorption (NH_3-TPD), H_2-temperature programmed reduction (H_2-TPR), pyridine Fourier Transform Infrared Spectroscopy (Py-FTIR), and energy dispersive spectroscopy (EDS). The ODHP behaviors of the samples were then assessed with and without CO_2 from 100 to 500 °C using Diffuse Reflectance Infrared Fourier Transform Spectroscopy (DRIFTS). Finally, the combined CO_2 capture and ODHP utilization performances were assessed from 600 to 700 °C, where the CaO/ZSM-5 (Ti) was found to produce the best balance of overall performance, achieving 76% CO_2 conversion and ~20% propylene yield. At the same time, however, the other dopants were shown to vary the distribution of CO_2/C_3H_8 conversion, C_3H_6 selectivity, and C_3H_6 yield, meaning that the technique reported herein should be considered a promising means of tuning the catalytic properties of structured DFM materials. Overall, this study contains two important aspects in that it both i) generates structured DFM adsorbent/catalyst materials of any kind and ii) successfully employs a DFM composite for combined CO_2 capture and ODHP reaction within a single bed. Notably, the second aspect is of high importance to the area of CO_2 capture and utilization, as there has not been a study which applies DFMs to propane dehydrogenation. Hence, this study reports an exciting pathway through which to utilize CO_2 and represents an impressive advancement in material science.

2. Experimental section

2.1. Materials

The following materials were purchased from Sigma Aldrich and were used for the formulation and characterization of 3D-printed adsorbent/catalyst monoliths without modification: Ga_2O_3 (99.9%), $CaCO_3$ (99%), V_2O_5 (98 +%), NiO (99%), TiO_2 (99%), methylcellulose (99%), bentonite clay, and pyridine (ACS). The H-ZSM-5 (SiAl = 30) was purchased from Zeolyst International and all ultra-high purity (UHP) gases were purchased from Airgas.

2.2. Monolith formulation

The paste ratios in Table 1 were 3D-printed using our established technique to formulate the DFM adsorbent/catalyst monoliths. [14–17] Briefly, the as-received powders were rolled at 60 rpm along with ~10 mL of DI water for 48 h at 25 °C to induce binding and achieve homogeneity. The inks were then heated at 60 °C for ~4 h to extract the water until a self-standing rheology was observed, where self-standing behavior is defined as that which retains layer separation after printing without fluidic spreading. [5] The printed monoliths were then dried for 12 h at 25 °C in the fume hood to prevent cracking, whereafter they were heated in air at 10 °C/min to 550 °C and calcined for 6 h. It should be clarified here that the $CaCO_3$ concentration in the printing inks was greater than 50 wt%; however, calcining the $CaCO_3$ into CaO resulted in a 50:50 split of adsorbent and catalyst.

2.3. DFM monolith characterization

The crystalline structures of the monoliths were assessed by X-ray diffraction (XRD) on a PANalytical X′Pert multipurpose X-ray diffractometer with a 0.02°/step scan size,137.2 s/step rate, and $5 < 2\theta < 50°$

Table 1
Paste ratios used for 3D printing DFM adsorbent/catalyst monoliths.

Sample	ZSM-5 (wt%)	$CaCO_3$ (wt%)	Bentonite Clay (wt%)	Methyl-cellulose (wt%)	V_2O_5 (wt%)	Ga_2O_3 (wt%)	TiO_2 (wt%)	NiO (wt%)
CaO/ZSM-5	29.0	59.0	10.0	2.0	0.0	0.0	0.0	0.0
CaO/ZSM-5 (V)	27.4	55.5	9.1	1.9	6.1	0.0	0.0	0.0
CaO/ZSM-5 (Ga)	27.4	55.5	9.1	1.9	0.0	6.1	0.0	0.0
CaO/ZSM-5 (Ti)	27.4	55.5	9.1	1.9	0.0	0.0	6.1	0.0
CaO/ZSM-5 (Ni)	27.4	55.5	9.1	1.9	0.0	0.0	0.0	6.1

range. The metal dispersions were assessed with energy dispersive spectroscopy (EDS) on a Quanta 600 F ESEM with Bruker Quantax EDS. The monolith textural properties were evaluated with N_2 physisorption at 77 K on a Micromeritics (3Flex) gas analyzer. The samples were degassed under vacuum at 350 ºC for 6 h on a Micromeritics SmartVac prep system prior to analysis and the surface area and pore volume were calculated from the physisorption data by the Brunauer-Emmet-Teller (BET) and non-local density functional theory (NLDFT) methods, respectively. We also employed a Micromeritics 3Flex instrument to assess the acidities, CO_2 bond strengths, and redox properties of the monoliths, using temperature-programmed ammonia desorption (NH_3-TPD), temperature-programmed CO_2 desorption (CO_2-TPD), and temperature-programmed hydrogen reduction (H_2-TPR), respectively. The pretreatment conditions for these measurements are located in our previous works. [18,19] As a supplement to H_2-TPR, we also assessed the valance states of the metal dopants using X-ray photoelectron spectroscopy (XPS) on a Thermoscientific Nexsa 128 channel XPS system. The scan voltage step for all metals was 0.1 eV and the scan conditions are located in Table 2. Meanwhile, the acid sites were further characterized using pyridine Fourier-Transform Infrared Spectroscopy (Py-FTIR) to better understand whether the catalysts were predominately Lewis or Brønsted acids. To this end, the samples were first degassed for 12 h under vacuum at 200 ºC to ward off any pre-adsorbed species. Then, they were sealed in glass jars with 10 mL of liquid pyridine and heated to 50 ºC for 12 h to produce pyridine vapor and saturate the active sites. Finally, the samples were characterized using a Nicolet iS50 FTIR equipped with an attenuated total reflectance (ATR) diamond to determine which type of acidity was most dominant.

2.4. C_3H_8-DRIFTS

The ODHP behavior of the DFM adsorbent/catalysts was assessed using in-situ C_3H_8- Diffuse Reflectance Infrared Fourier Transform Spectroscopy (DRIFTS) as a function of temperature (100–500 ºC) in both the presence and absence of CO_2 to determine i) how the composite materials behave in ODHP reactions, ii) how the metal-dopant effects ODHP performance, and iii) how the presence of CO_2 influences the reactionary behavior. A Nicolet iS-10 FTIR spectrometer (Thermo Fisher Scientific, Waltham, MA, USA) was utilized with a catalytic reaction cell attachment (Harrick Scientific, Pleasantville, NY, USA). Prior to each analysis, samples were crushed into a fine powder. Each catalyst was subjected to a temperature ramp and soak in 120 mL/min of He (UHP, Airgas) to 500 °C with holding for 15 min prior to pretreatment with 21%O_2/79%N_2 (UHP, Airgas) at 50 mL/min. Then, the system was again purged with 120 mL/min of He and background scans were collected at T = 500, 300, and 100 °C. Finally, 100 mL/min of the reactant stream mixture – either 5%C_3H_8/95%N_2 or 5%C_3H_8/5%CO_2/90%N_2 – was flown through the cell and scans were collected at T = 100, 300, and 500 °C. It should be noted here that 500 °C was the upper limit of DRIFTS because that was the maximum temperature of the thermal cell.

Table 2
XPS scan conditions used to assess the valance states of metal-oxide dopants in DFM adsorbent/catalyst monoliths.

Sample	Orbital Scan	Number of Scans	Scan Time (sec)	Voltage range (eV)
CaO/ZSM-5 (V)	V-2p	20	281	507–535
CaO/ZSM-5 (Ni)	Ni-2p	30	601.5	844–884
CaO/ZSM-5 (Ti)	Ti-2p	30	406.5	448–475
CaO/ZSM-5 (Ga)	Ga-3d	10	85.5	15–32

2.5. Combined adsorption/catalysis experiments

The CO_2 adsorption capacities of the samples were collected via thermogravimetric analysis on a Q500 thermogravimetric gas analyzer (TGA) from TA instruments. Therein, the samples were first heated under 40 mL/min of N_2 at 10 ºC/min to 750 ºC. After 1 h, the system was cooled to 600 ºC and the sample was saturated for 90 min with 60 mL/min of 500 ppm to 10% CO_2/N_2. The combined adsorption/catalysis performances were assessed using our established setup for propane dehydrogenation. [15,17] In each experiment, 0.2 g of the DFM monolith was packed into the reactor with quartz wool. The dimensions of a typical sample are shown in Fig. 1. The adsorption/catalysis experiments were performed in a similar way to those reported in our previous work for combined CO_2 capture and utilization for ethane dehydrogenation. [10] Briefly, the bed was heated under 25 mL/min of Ar at 10 ºC/min to 700 ºC for 1 h to desorb CO_2 from the CaO adsorbent. The reactor was then cooled to 600 ºC, after which the sample was saturated with 20 mL/min of 500 ppm to 10% CO_2/Ar for 1 h. While keeping under CO_2 flow, the system was then heated to the target reaction temperature at a rate of 10 ºC/min. To fully optimize the reaction conditions, CO_2 desorption coupled with ODHP was performed at temperatures of 600, 650, and 700 ºC. Upon reaching the reaction temperature, the CO_2 feed was terminated and 20 mL/min of 5% C_3H_8/Ar was allowed to flow into the reactor. The effluent concentrations of the various species were analyzed by an MKS Cirrus 2 Mass Spectrometer throughout the entirety of the adsorption/reaction experiments.

3. Results and discussion

3.1. Characterization of DFM monoliths

The monoliths' N_2 physisorption isotherms and NLDFT pore distributions (offset for clarity) are shown in Fig. 2. The corresponding textural properties are contained in Table 3. From Fig. 2a, all samples displayed Type-II physisorption behavior with Type-H_4 hysteresis which signals microporous texture as denoted by the IUPAC. [20] This behavior was anticipated because ZSM-5 is a known microporous zeolite, however, it should be noted that the isotherms for the V- and Ti-doped samples showed higher slopes than the other three catalysts. This behavior coincides with increased multilayer adsorption on the material surface instead of monolayer adsorption inside the internal micro/mesopores. [21] Generally, such behavior indicates some malformation of the bulk pore shape, so this result suggested that the ZSM-5 in these samples underwent some physiochemical change. [22] The pore distributions (Fig. 2b) further confirmed this theory because the V- and Ti-doped samples displayed more mesopore space than the other monoliths. It is difficult to predict how such changes will influence catalytic behavior given that our previous work indicated that V/ZSM-5

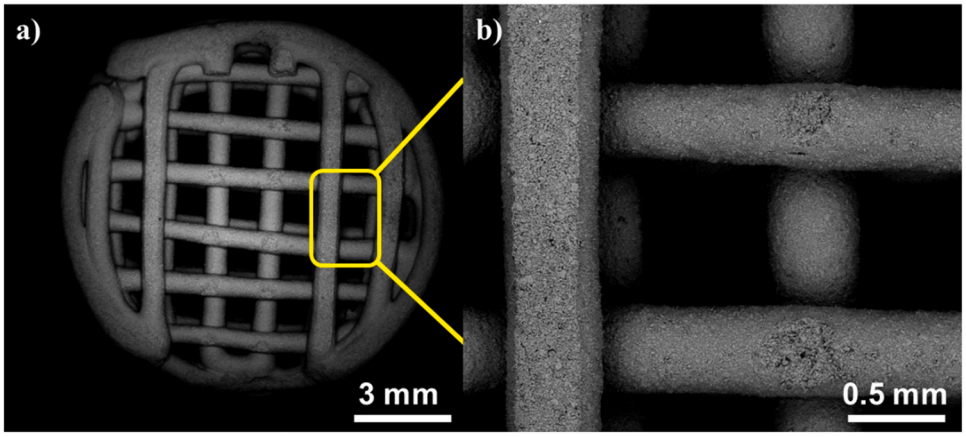

Fig. 1. SEM micrographs of (a) monolith top view and (b) channel dimensions for 3D-printed DFM adsorbent/catalysts.

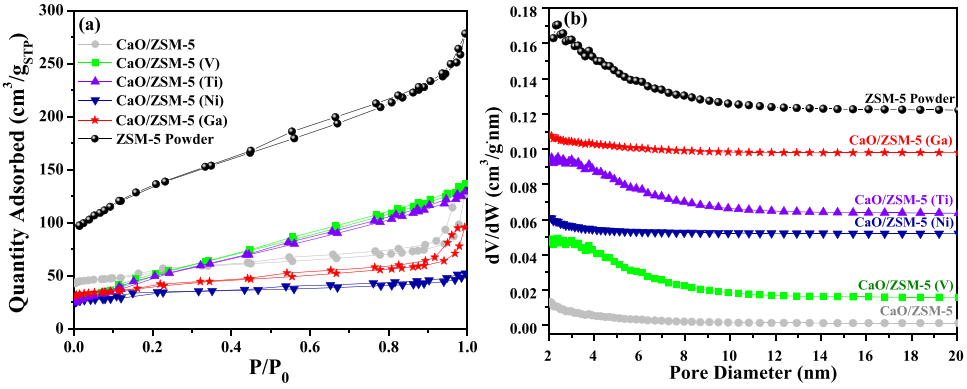

Fig. 2. (a) N_2 physisorption isotherms and (b) NLDFT pore distributions for 3D-printed DFM adsorbent catalyst monoliths.

Table 3
Textural properties of DFM catalysts with V-, Ga-, Ti-, and Ni-dopants.

Sample	S_{BET} (m^2/g)	$V_{p\text{-micro}}$ (cm^3/g)	$V_{p\text{-meso}}$ (cm^3/g)	Pore Diameter (nm)
ZSM-5 Powder	470	0.16	0.22	2.5
CaO/ZSM-5	180	0.07	0.08	2.0
CaO/ZSM-5 (V)	210	0.03	0.07	2.0–8.0
CaO/ZSM-5 (Ga)	140	0.05	0.07	2.0
CaO/ZSM-5 (Ti)	200	0.03	0.15	2.0–8.0
CaO/ZSM-5 (Ni)	120	0.04	0.03	2.0

catalysts with low surface area and pore volume had higher acid site concentrations which enhanced ODHP activity, [14,15,17] whereas results reported in the open literature have indicated that higher surface area catalysts have more accessible active sites and enhanced catalytic properties. [23–27] Therefore, no predictions pertaining to the ODHP performances of these catalysts could be drawn from the textural properties; however, Fig. 2 and Table 3 both indicated some degree of textural change for the V- and Ti-doped samples within the ZSM-5 phase.

The monolith crystallinities and metal dopant dispersions were assessed by XRD and EDS as shown in Fig. 3. From the XRD (Fig. 3a), the Ti-, Ni-, and V-doped samples displayed a diffractive peak at $2\theta = 29$ ° with varying intensities which corresponds to the [104] plane of $CaCO_3$. [28] The presence of this peak did not indicate that calcination at 550 °C failed to remove CO_3^{2+} ion, but likely signified that the samples

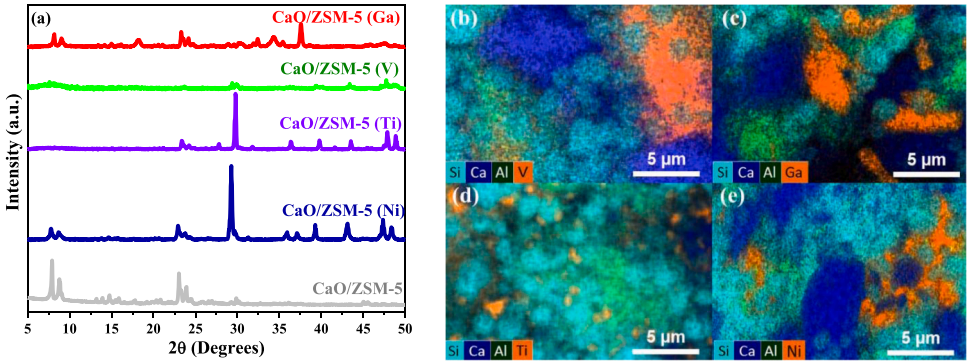

Fig. 3. (a) XRD spectra and composite EDS maps for (b) CaO/ZSM-5 (V), (c) CaO/ZSM-5 (Ga), (d) CaO/ZSM-5 (Ti), and (e) CaO/ZSM-5 (Ni).

adsorbed CO_2 during cooling. This conclusion is reasonable because the calcination was performed in air, meaning that some degree of CO_2 adsorption should be expected. As per the differences in the [104] $CaCO_3$ peak intensities across samples, these likely stimmed from differences in the furnace environment. Namely, because atmospheric air was used in the furnace and there was no control of the air flowrate, it is reasonable that some samples – in this case $CaCO_3$/ZSM-5 (Ni) and $CaCO_3$/ZSM-5 (Ti) – would be exposed to more CO_2 during cooling than others. Therefore, the [104] plane was not considered to be significant. On the other hand, the differences in ZSM-5 diffractive indices between the various metal dopants indicated that some metal-oxides interacted with the zeolite phase. First looking at the retained peaks, CaO/ZSM-5 as well as the Ga- and Ni-doped monoliths showed diffractive peaks at $2\theta = 7.5\,°$, $8.8\,°$, $22.5\,°$, and $49\,°$ which are consistent with the ZSM-5 diffractive pattern. [18] These peaks were mostly present in the V- and Ti-doped samples as well; however, there were losses in diffractive intensity at $2\theta = 7.5\,°$ and $8.8\,°$, suggesting that these dopants reacted to some degree with the ZSM-5 during calcination. Such losses in crystallinity could be anticipated for V_2O_5 because ZSM-5 is prone to dealumination by Si-OH hydration with VO_x; however, we were unable to find any reports of this behavior occurring for TiO_2. [14,17,29] That said, these losses in XRD intensity for the V- and Ti-doped samples did agree with the physisorption data in Fig. 2, so the XRD patterns confirmed that there was some interaction between V_2O_5 and ZSM-5 as well as TiO_2 and ZSM-5 during calcination. Granted, the crystallinity of the ZSM-5 is not the only factor which influences catalytic behavior, as metallic dispersion, redox properties, and acidity/basicity are also important. In this regard, the EDS maps also signified that there were differences in metal dispersion across the samples. For example, CaO/ZSM-5 (V) (Fig. 3b) and CaO/ZSM-5 (Fig. 3d) displayed a greater amount of clustering behavior and larger metal phases whereas CaO/ZSM-5 (Ti) (Fig. 3c) and CaO/ZSM-5 (Ga) (Fig. 3e) displayed a higher dispersion. Between the two, the Ti-doped samples showed smaller particles; thus, it likely had the best contact between the bifunctional catalyst phases of all the samples. It could not be said for certain how such dispersions would affect the catalytic behavior, only

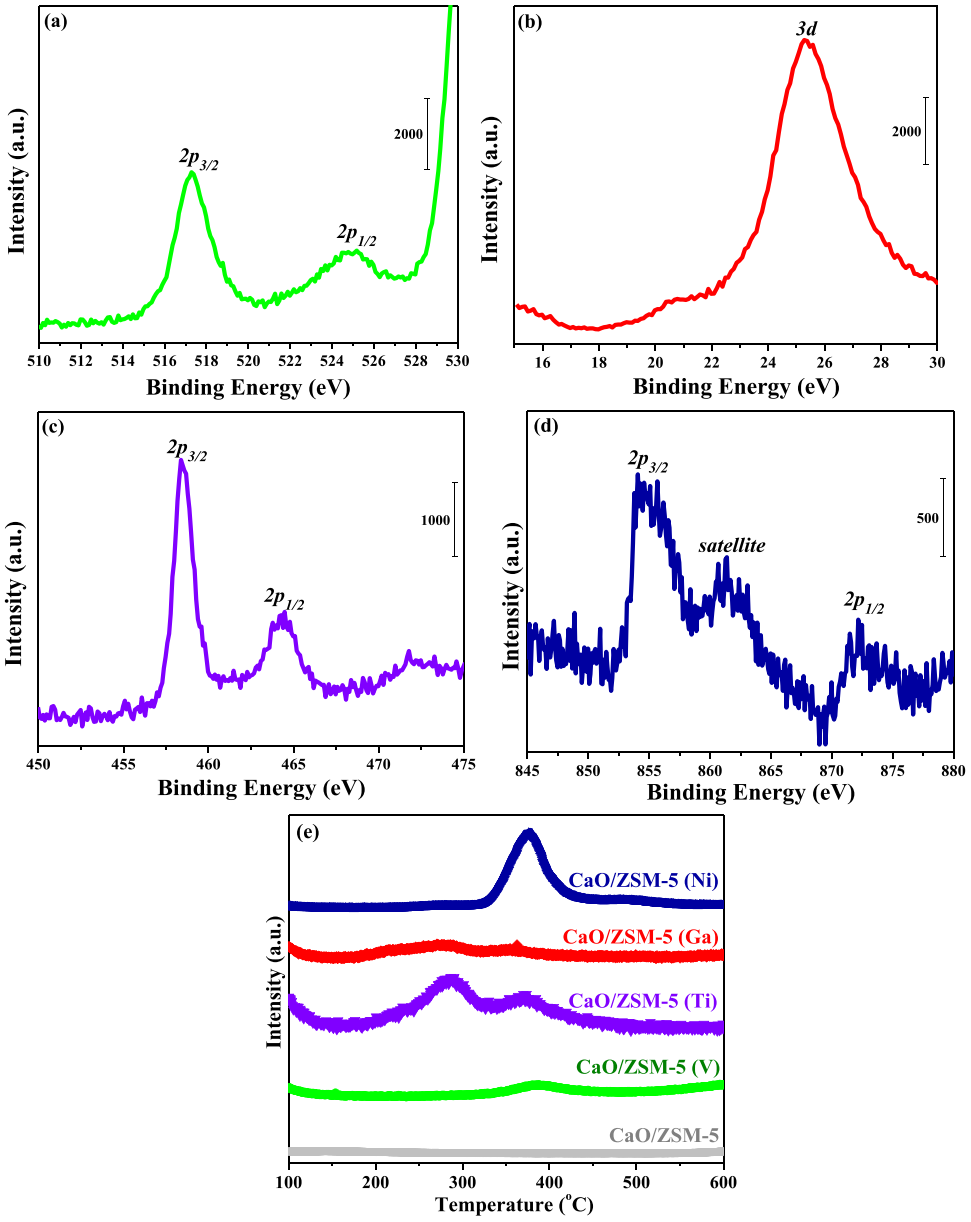

Fig. 4. XPS spectra for 3D-printed (a) CaO/ZSM (V), (b) CaO/ZSM-5 (Ga), (c) CaO/ZSM-5 (Ti), and (d) CaO/ZSM-5 (Ni) adsorbent/catalyst monoliths as well as (e) corresponding H_2-TPR profiles.

that the dispersion of titania was the highest of the four dopants within the localized areas that were examined by EDS.

3.2. Characterization of DFM monolith redox properties

The monolith redox properties were assessed by H_2-TPR and the metallic valance states were further characterized by XPS. As shown in Fig. 4, the samples all displayed reductive behaviors which were consistent with their individual metal-oxide dopants. For example, CaO/ZSM-5 (Fig. 4a) displayed peaks at 516 and 525 eV which correspond to the $2p_{3/2}$ and $2p_{1/2}$ orbitals, respectively. [30,31] Meanwhile, CaO/ZSM-5 (Ga) (Fig. 4b) displayed a peak at 25.5 eV which corresponds to the 3d orbital of Ga^{3+}, [32] whereas CaO/ZSM-5 (Ti) (Fig. 4c) displayed peaks at 458.5 eV and 464.4 eV which correspond to the $2p_{3/2}$ and $2p_{1/2}$ orbitals, respectively. [33] Finally, CaO/ZSM-5 (Ni) (Fig. 4d) displayed peaks at 855 eV and 872.5 eV which are consistent with the $2p_{3/2}$ and $2p_{1/2}$ orbitals, respectively. [34] Again, given that these orbital peaks were all consistent with the valance states of the metal dopants, the XPS spectra signified that the printing and calcination process did not affect the metal oxidation states. However, the H_2-TPR signified that there was some synergistic effect which occurred pertaining to the metals' reductive behaviors upon formulating these materials into monoliths.

To be more specific, it was observed in Fig. 4e that some samples showed lower reduction temperatures than are typically reported in literature. For example, the V-doped sample displayed reductive peaks at the typical temperature of 350–400 °C, which corresponds to V_2O_5 reduction into VO_2, while the Ni-doped sample displayed the typical reductive peak for Ni^{2+} into Ni^0 that occurs at 380 °C. [35] While these peaks were anticipated from the open literature, the Ga- and Ti-doped samples displayed different reductive behaviors than expected. Namely, the Ga-doped sample displayed peaks at 200–300 °C and 350 °C which correspond to various modes of reduction that occur when Ga^{3+} partially substitutes on ZSM-5. [36] Meanwhile, the Ti-doped sample displayed reductive peaks at 275 °C and 375 °C, which are ascribed to various modes of Ti^{2+} reduction into Ti^0 but usually occur at ~475 °C. [37] In CaO/ZSM-5 (Ti), this synergistic reductive behavior likely stemmed from the high TiO_2 dispersion which was observed in EDS; however, the partial Ga^{3+} substitution was not apparent from either XRD, XPS, or the physisorption data. Thus, it was unlikely to be caused by partial substitution into ZSM-5 and probably resulted from some innate change in the physiochemical property of the metal-dopant itself. While it is difficult to pinpoint exactly what this change was, it could be stated for certain that some synergism occurred upon doping Ga into our DFM materials. Having said this, such effects could not be directly related to the ODHP performance of these materials in the presence of CO_2 within a single bed because i) combined CO_2 capture and propane dehydrogenation in a singular bed have never been reported before and ii) the overall catalytic performance depends on many factors, not just the redox properties of the metal.

3.3. Characterization of DFM monolith acidities

A combination of NH_3-TPD and Py-FTIR was used to characterize the acidities of the monoliths, as shown in Fig. 5. From the NH_3-TPD profiles (Fig. 5a), the bare, V-, Ni-, and Ti-doped samples all had both weak and strong acid sites, as evidenced by the peaks centered at ~170 °C and 650 °C, respectively. On the other hand, the Ga-doped monolith only displayed the weak acid site peak, signifying that Ga_2O_3 reduced the catalytic acidity. This reduction in acidity for the Ga-doped sample was somewhat expected, given that Ga_2O_3 is amphoteric and can act as both an acid and a base; as such, it is capable of reducing the catalytic acidity. [38] Given that this combined CO_2 capture and utilization for ODHP at 700 °C over a singular dual-functional composite has never been attempted before, it could not be speculated how this reduction in acidity would influence the performance of the catalyst. However, it could be said with certainty that CaO/ZSM-5 (Ga) was the least acidic sample whereas the other monoliths were of similar acidities. Of course, the catalytic behavior not only depends on the overall acidity but also relies on the type of acid site present. To this end, the Py-FTIR (Fig. 5b) spectra signified that all samples had both Lewis and Brønsted acid sites. Between these, most of the acid sits were Lewis sites as evidenced by the strong vibrational band at 1425 cm^{-1}, which was expected because ZSM-5 (the primary catalyst phase) is a known Lewis acid. [39] In contrast, the metal dopants impart varying degrees of both Lewis and Brønsted acidity, which yielded the mixture of acid sites present in the samples. It is also worth noting here that Ga_2O_3 doping did not change the type of acid site present, as it only influenced the acid site strengths. In this regard, it was concluded from Fig. 5 that the Ga-doped sample was the least acidic and all monoliths contained primarily Lewis acid sites but had low concentrations of Brønsted acid sites. The presence of the latter indicated that the monoliths did have bifunctional properties, however, the weak intensity of the Brønsted acid bands relative to the Lewis acid bands also indicated that the materials primarily could be considered Lewis acid catalysts, albeit Lewis acid catalysts which contained varying small degrees of Brønsted acidity.

3.4. DRIFTS

The propane dehydrogenation behaviors as a function of temperature for the different catalysts were assessed with and without CO_2 from 100 to 500 °C, as shown in Fig. 6. First, it should be noted that in both the presence and absence of CO_2, all samples displayed vibrational bands at 2144 and 1934 cm^{-1}, which both signify CO formation and attachment to the catalyst phases. [40] Notably, this vibration occurred both with and without CO_2, indicating that under either mode the DFM materials generated C-O attachment with propane. Between these, the CO bands were of higher intensity when CO_2 was present, signifying that

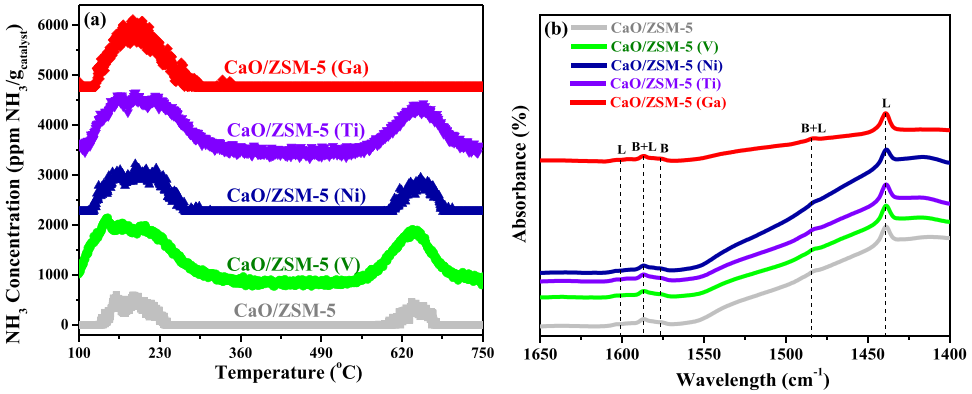

Fig. 5. (a) NH_3-TPD profiles and (b) Py-FTIR spectra of 3D-printed adsorbent/catalyst monoliths.

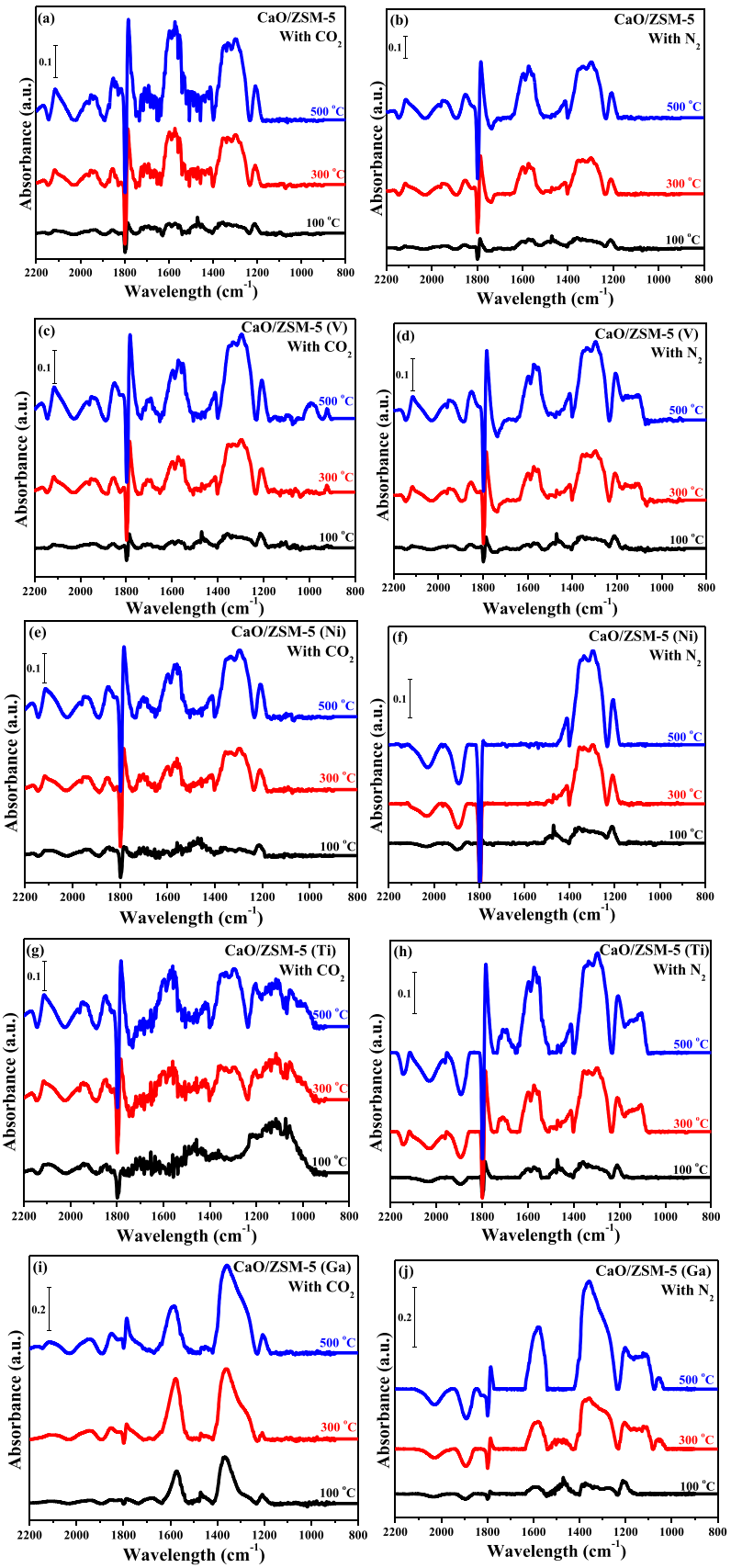

Fig. 6. Propane-DRIFTS profiles with (left) and without (right) CO_2 over (a-b) undoped, (c-d) V-doped, (e-f) Ni-doped, (g-h) Ti-doped, and (i-j) Ga-doped 3D-printed DFM monoliths.

the environment in the reactor was more oxidative under this condition. That said, the presence of CO when CO_2 was absent signified that the DFMs acted as oxidative sources in and of themselves, which likely stemmed from both the metal dopants as well as from the bentonite clay binder. From where this property arises is certainly debatable, but the fact that CO was generated when metal dopants were not present (Fig. 6b) suggested that it is innate to the CaO/bentonite/ZSM-5 composite phase, but could be further promoted by the metal dopants.

Moving onto the actual ODHP behavior, it should first be noted that all samples also displayed vibrational modes between 1800 and 1200 cm^{-1} (1750, 1700, 1600, 1425, 1350, and 1200 cm^{-1}) which correspond to various gas-phase vibrations of propane and CO_2 (C═O, C═O, C═O, CH_2-CH_3, C-H, and C-C bands, respectively). [41,42] Given that these vibrational modes were consistent with the propane feed, most of the discussion is focused on differences in the characteristic vibrational bands for propylene, which occur below 1200 cm^{-1}. Notably, these characteristic peaks were not present under either mode of reaction in the undoped (Figs. 6a–6b), Ni-doped (Figs. 6e–6f), or Ga-doped (Figs. 6i-6j) samples; however, the V-doped (Figs. 6c–6d), and Ti-doped monoliths (Figs. 6g–6h) displayed vibrational bands which mark the presence of C_3H_6. Namely, these samples both displayed a vibrational mode at 1026 cm^{-1} in the presence of CO_2 which coincides with allylic attachment of propylene to metal-oxides (i.e., CH_2 =CH-CH_2-OH attachment). [43] It should be noted here that, because this band signals the presence of propylene, it could be reasonably claimed that propylene formation over the V- and Ti-doped catalysts occurred more favorably. However, it is possible that the temperature of 500 °C was simply not enough to overcome the activation barrier for the other samples, so the DRIFTS spectra did not discount the bare, Ni-, and Ga-doped materials as potential DFM catalysts. It should also be noted here that removing CO_2 generated differences in the DRIFTS spectra for the V- and Ti-doped samples between 1150 and 1080 cm^{-1}. Specifically, a new peak appeared in this wavelength for CaO/ZSM-5 (V), whereas it heightened in intensity for the Ti-doped sample. Given that this peak is known to signal bidentate carbonate formation on bifunctional active sites, these trends suggested an increase in coking when CO_2 was absent. [44] A similar effect was observed for CaO/ZSM-5 (Ga) upon removing CO_2 from the feed; however, given that this sample failed to produce propylene, the novel vibrational band from 1150 to 1080 cm^{-1} likely indicated carbonate formation via thermal cracking. These findings suggested that the Ga-doped sample would not effectively utilize CO_2 for the ODHP reaction, since this sample showed a propensity towards thermal cracking. Indeed, this was corroborated by the experimental capture/conversion experiments in Section 3.5. In any case, the DRIFTS

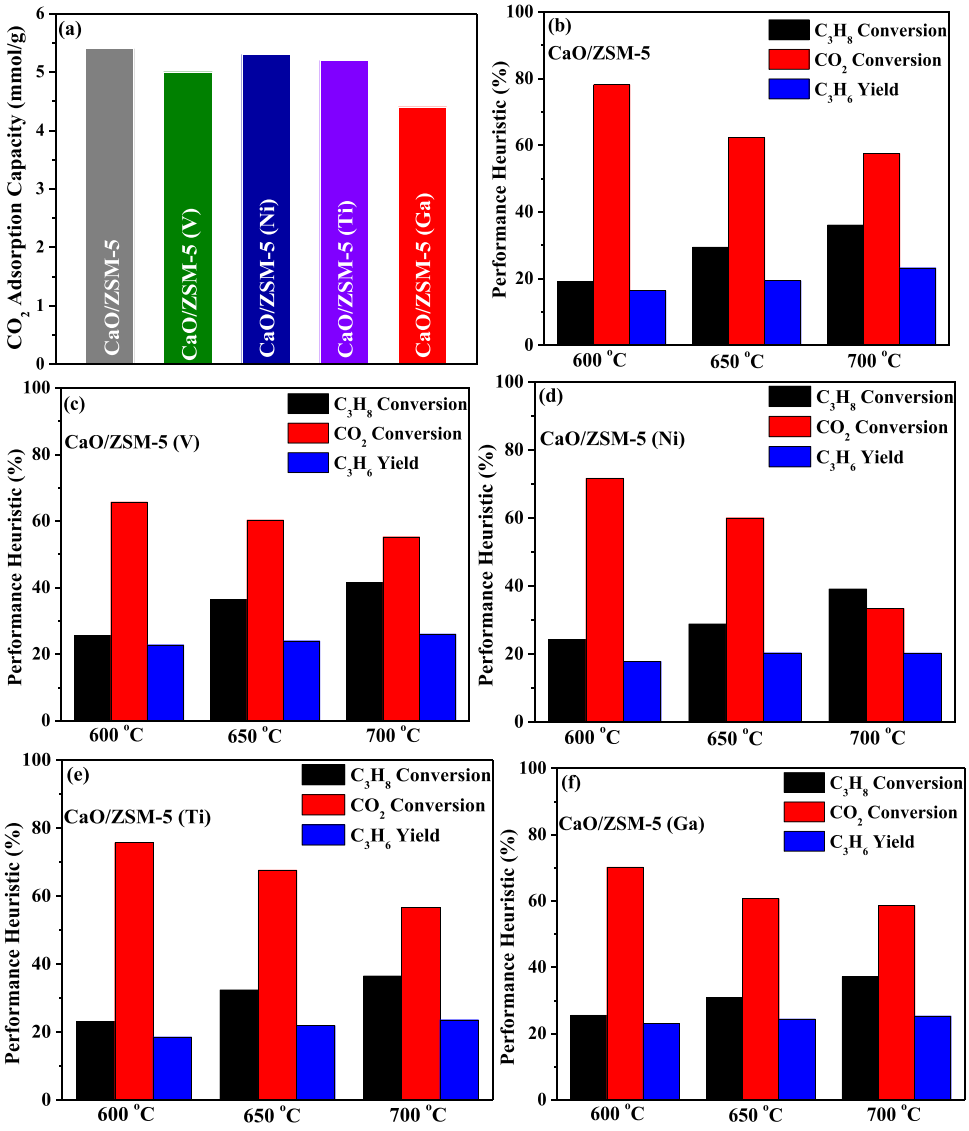

Fig. 7. (a) CO_2 adsorption capacities for each sample from TGA analysis at 600 °C as well as adsorption/reaction performances as a function of temperature for (b) CaO/ZSM-5, (c) CaO/ZSM-5 (V), (d) CaO/ZSM-5 (Ni), (e) CaO/ZSM-5 (Ti), and (f) CaO/ZSM-5 (Ga).

experiments did indicate profound differences in catalytic behavior across the various catalysts, where the propylene synthesis was suggested to occur most favorably over the V- and Ti-doped samples.

3.5. Combined adsorption/catalysis experiments

The combined CO_2 capture/conversion experimental results are shown in Fig. 7 and the corresponding dataset is summarized in Table 4. For reference, the actual concentration profiles from the adsorption/reaction experiments are located in Figs. S2-S6, Supporting Information. Here, it should be noted that the mass spectrometric profiles displayed signal noises which were less than a fraction of a percent, so the differences in performances across the catalysts regarding the conversions, selectivities, and propylene yields were considered accurate with a high degree of confidence. As evident from Fig. 7a, most of the samples displayed similar CO_2 adsorption capacities; however, there was a slight decrease for the Ga-doped sample. That being said, the reduced capacity in CaO/ZSM-5 (Ga) was not too far removed from the other samples, so it is likely that this was merely caused by random error between samples. In this regard, the TGA measurements indicated that the metal dopant does not greatly affect the CO_2 adsorption capacity of the DFM monolith. That said, there were profound differences in the behaviors of the samples in the combined adsorption/catalysis experiments.

From these, it should first be noted that the highest CO_2 conversion was observed in the undoped sample (Fig. 7b); however, this sample also generated the lowest propylene yield at all conditions, whereas the metal-doped samples improved on this aspect. Hence, there was a clear benefit of the metal doping. Between the various samples, the V-doped sample consistently generated the highest propylene yield, owing to the high acidity and numerous oxidative states of VO_x. [45] Nevertheless, CaO/ZSM-5 (V) displayed lower CO_2 conversion than the other monoliths – with the highest balance of CO_2 conversion (e.g., 76%) and C_3H_6 yield (e.g., 19%) being present in CaO/ZSM-5 (Ti) – meaning that a great deal of the V_2O_5-doped sample's activity was likely caused by thermal cracking. This was consistent with the high activity of this catalyst at the low temperature of 500 °C as observed in the DRIFTS spectra, so it may be worth exploring CaO/ZSM-5 (V) at lower ODHP temperatures in subsequent studies. Otherwise, it may be worth doping CaO/ZSM-5 (V) with TiO_2 to harness both the oxidative behavior of titania as well as the catalytic behavior of vanadia to maintain the fully isothermal condition presented here. At the same time, one could also dope small amounts of Ga_2O_3 to enhance the propylene selectivity. Such work should be the target of a follow-up study as this work focuses on development of an initial metal screening and expanding DFMs to ODHP applications. Regarding this goal, Fig. 7 clearly indicated that DFMs can be expanded to combine CO_2 adsorption/ODHP within a single bed, displaying similar efficacy to ethane dehydrogenation applications. [10] It is also worth noting here that, unlike our previous work where the reaction step occurred at 700 °C to ensure desorption of CO_2, the catalysts in this study generated their best performance with adsorption and catalysis both occurring at 600 °C, whereas swinging between the 600 °C adsorption temperature and higher catalysis temperatures caused a shift towards thermal cracking. In this aspect, the materials in this study improved upon that which was reported previously for double-salt DFMs, [10] as the 3D-printed monoliths were capable of completely performing both processes at the same temperature which eliminated the thermal gradient compared to combined adsorption/catalysis processes from DFMs for ODHE applications. In summary, combined adsorption/catalysis experiments displayed in Fig. 7 display an exceptionally promising proof-of-concept for the use of structured DFM materials.

4. Conclusions

In this study, we expanded the idea of DFM adsorbent/catalyst materials to ODHP applications and simultaneously manufactured the first-ever iteration of structured DFM monoliths. As was demonstrated by the vigorous characterization protocol, the metal dopant was found to considerably influence the catalytic properties of the catalytic monolith, as there were clear distinctions between the acidities, dispersions, and redox properties across the different monoliths. By extension, such differences led to subtle changes in catalytic behavior for the DFMs in the combined CO_2 capture/ODHP reaction process at all three temperatures. From these experiments, it was determined that the Ti-doped sample generated the best balance of propylene yield and CO_2 conversion at the specific condition of 600 °C; however, the experiments also suggested that including V_2O_5 as a co-dopant could further enhance catalytic activity. Meanwhile, the experiments indicated that Ga-doped DFMs should be used if high propylene selectivity is desired and CO_2 conversion is not necessary. In this way, this study indicates that this technique, namely structuring DFM materials by 3D printing $CaCO_3$/metal oxide/ZSM-5 inks, is a facile way of tuning the properties of the composite materials. Furthermore, the various ODHP runs revealed that the samples generate the best CO_2 capture/conversion performance when both steps are performed at 600 °C, thus fully eliminating the thermal gradient which normally occurs between the two processes. Therefore, this study demonstrates a promising novel route through which to utilize CO_2 that is both marketable and energetically efficient, meaning that the work culminated herein should be considered a significant advancement in material science, CO_2 utilization, and light olefin manufacturing.

Table 4
Summary of product distributions for combined adsorption/catalysis ODHP experiments over 3D-printed CaO/ZSM-5 monoliths with various metal dopants.

Sample	Reaction Temperature (°C)	C_3H_8 Conversion (%)	CO_2 Conversion (%)	C_3H_6 Yield (%)	C_3H_6 Selectivity (%)	C_2H_4 Selectivity (%)	CH_4 Selectivity (%)	CO Selectivity (%)	H_2 Selectivity (%)	H_2O Selectivity (%)
CaO/	600	19.1	78.1	16.3	36.7	0.0	18.4	26.4	7.5	11.0
ZSM-5	650	29.4	62.3	19.3	13.2	21.6	15.6	15.8	25.1	8.7
	700	36.0	57.5	23.2	6.23	26.5	21.7	20.6	21.1	4.0
CaO/	600	25.6	65.6	22.8	25.2	1.2	12.1	21.8	18.2	21.5
ZSM-5	650	36.4	60.3	24.0	16.3	14.5	14.4	16.6	24.0	14.2
(V)	700	41.5	55.2	26.0	8.9	22.1	22.1	21.7	21.4	3.9
CaO/	600	24.2	71.2	17.8	9.7	28.0	7.4	5.2	46.5	3.2
ZSM-5	650	28.8	60.0	20.3	5.8	27.6	8.2	13.3	35.1	9.9
(Ni)	700	39.1	33.3	20.2	3.8	25.1	20.1	6.9	35.9	8.2
CaO/	600	23.1	75.7	19.0	39.0	1.0	14.8	22.0	15.6	7.6
ZSM-5	650	32.4	67.6	21.9	19.8	21.3	25.7	9.1	22.9	1.3
(Ti)	700	36.5	56.7	23.6	7.5	26.5	21.9	23.4	18.4	2.3
CaO/	600	25.5	70.2	23.0	42.0	1.3	15.6	22.0	7.2	12.0
ZSM-5	650	30.8	60.7	24.4	22.5	11.9	16.1	21.8	15.4	12.4
(Ga)	700	37.2	58.6	25.3	7.0	22.7	19.0	10.7	36.4	4.3

CRediT authorship contribution statement

Shane Lawson: Methodology, Investigation, Visualization, Writing – original draft. **Khaled Baamran:** Methodology, Resources, Data curation, Review & editing. **Kyle Newport:** Methodology, Resources, Review & editing. **Turki Alghamadi:** Methodology, Resources, Review & editing. **Gary Jacobs:** Methodology, Validation, Review & editing. **Fateme Rezaei:** Conceptualization, Methodology, Writing – review & editing, Supervision, Funding acquisition. **Ali A. Rownaghi:** Conceptualization, Methodology, Writing – review & editing, Project administration, Funding acquisition.

Declaration of Competing Interest

The authors declare that they have no known competing financial interests or personal relationships that could have appeared to influence the work reported in this paper.

Acknowledgements

The authors acknowledge the materials research center (MRC) at Missouri University of Science and Technology for performing the XRD and XPS characterizations as well as the electron microscopy core (EMC) at University of Missouri Columbia for taking the backscatter images and elemental maps. The involvement of Shane Lawson in this work was sponsored by the National Science Foundation internship program (NSF CBET-1802049).

Appendix A. Supporting information

Supplementary data associated with this article can be found in the online version at doi:10.1016/j.apcatb.2021.120907.

References

[1] A. Al-Mamoori, A. Krishnamurthy, A.A. Rownaghi, F. Rezaei, Carbon capture and utilization update, Energy Technol. 5 (2017) 834–849.
[2] C. Jeong-aPotter, R. Farrauto, Feasibility study of combining direct air capture of CO_2 and methanation at isothermal conditions with dual function materials, Appl. Catal. B: Environ. 282 (2021), 119416.
[3] F. Zeng, C. Mebrahtu, X. Xi, L. Liao, J. Ren, J. Xie, H.-J. Heeres, R. Palkovits, Catalysts design for higher alcohols synthesis by CO_2 hydrogenation: trends and future perspectives, Appl. Catal. B: Environ. 291 (2021), 120073.
[4] T. Gelles, S. Lawson, A. Rownaghi, F. Rezaei, Recent advances in development of amine functionalized adsorbents for CO_2 capture, Adsorption 26 (2020) 5–50.
[5] M.S. Duyar, M.A.A. Treviño, R.J. Farrauto, Dual function materials for CO_2 capture and conversion using renewable H2, Appl. Catal. B: Environ. 168–169 (168–169) (2015) 370–376.
[6] A.M. Bahmanpour, M. Signorile, O. Krocher, Recent progress in syngas production via catalytic CO_2 hydrogenation reaction, Appl. Catal. B: Environ. 295 (2021), 120319.
[7] A. Dokania, A. Ramirez, A. Bnastasiya, J. Gascon, Heterogeneous catalysis for the valorization of CO_2: role of bifunctional processes in the production of chemicals, ACS Energy Lett. 4 (2019) 167–176.
[8] M.A. Atanga, F. Rezaei, A. Jawad, M. Fitch, A.A. Rownaghi, Oxidative dehydrogenation of propane to propylene with carbon dioxide, Appl. Catal. B: Environ. 220 (2018) 429–445.
[9] R.T. Hannagan, G. Giannakakis, R. Réocreux, J. Schumann, J. Finzel, Y. Wang, A. Michaelides, P. Deshlahra, P. Christopher, M. Flytzani-Stephanopoulos, M. Stamatakis, E.H. Sykes, First-principles design of a single-atom–alloy propane dehydrogenation catalyst, Science 372 (2021) 1444–1447.
[10] A. Al-mamoori, S. Lawson, A.A. Rownaghi, F. Rezaei, Oxidative dehydrogenation of ethane to ethylene in an integrated CO_2 capture-utilization process, Appl. Catal. B: Environ. 278 (2020), 119329.
[11] A. Cherevotan, J. Raj, L. Dheer, S. Roy, S. Sarkar, R. Das, C.P. Vinod, S. Xu, P. Wells, U.V. Waghmare, S.C. Peter, Operando generated ordered heterogeneous catalyst for the selective conversion of CO_2 to methanol, ACS Energy Lett. 6 (2021) 509–516.
[12] A. Porta, C.G. Visconti, L. Castoldi, R. Matarrese, C. Jeong-potter, R.J. Farrauto, L. Lietti, Ru-Ba synergistic effect in dual functioning materials for cyclic CO_2 capture and methanation, Appl. Catal. B: Environ. 283 (2021), 119654.
[13] S. Lawson, X. Li, H. Thakkar, A.A. Rownaghi, F. Rezaei, Recent advances in 3D printing of structured materials for adsorption and catalysis applications, Chem. Rev. 121 (2021) 6246–6291.
[14] S.J. Park, M. Bukhovko P., C. Jones W., Integrated capture and conversion of CO_2 into methane using NaNO3/MgO + Ru/Al2O3 as a catalytic sorbent, Chem. Eng. J. 420 (2021), 130369.
[15] S. Lawson, K.A. Newport, A. Axtell, C. Boucher, B. Grant, M. Haas, M. Lee, F. Rezaei, A. Rownaghi, Structured bifunctional catalysts for CO_2 activation and oxidative dehydrogenation of propane, ACS Sustain. Chem. Eng. 9 (2021) 5716–5727.
[16] F. Magzoub, S. Lawson, F. Rezaei, A.A. Rownaghi, Directly printed oxide/ZSM 5 bifunctional catalysts for methanol conversion to dimethyl ether with exceptional stability, conversion, and selectivity, Energy Fuels 35 (2021) 2619–2629.
[17] T. Alghamdi, K. Baamran, M.U. Okoronkwo, A. Rownaghi, F. Rezaei, Metal-doped K-Ca double salts with improved capture performance and stability for high-temperature CO_2 adsorption, Energy Fuel 35 (2021) 4258–4266.
[18] X. Li, F. Rezaei, A. Rownaghi, Methanol-to-olefin conversion on 3D-printed ZSM-5 monolith catalysts: effects of metal doping, mesoporosity and acid strength, Microporous Mesoporous Mater. 276 (2019) 1–12.
[19] F. Magzoub, X. Li, J. Al-darwish, F. Rezaei, A.A. Rownaghi, 3D-printed ZSM-5 monoliths with metal dopants for methanol conversion in the presence and absence of carbon dioxide, Appl. Catal. B: Environ. 245 (2019) 486–495.
[20] M. Thommes, K. Kaneko, A.V. Neimark, J.P. Olivier, F. Rodriguez-Reinoso, J. Rouquerol, K.S.W. Sing, Physisorption of gases, with special reference to the evaluation of surface area and pore size distribution (IUPAC Technical Report), Pure Appl. Chem. 87 (2015) 1051–1069.
[21] K.S.W. Sing, Physisorption of nitrogen by porous materials, J. Porous Mater. 2 (1995) 5–8.
[22] S. Storck, H. Bretinger, W.F. Maier, Characterization of micro- and mesoporous solids by physisorption methods and pore-size analysis, Appl. Catal. A: Gen. 174 (1998) 137–146.
[23] L.L. Shen, K. Xia, W.Z. Lang, L.F. Chu, X. Yan, Y.J. Guo, The effects of calcination temperature of support on PtIn/Mg(Al)O catalysts for propane dehydrogenation reaction, Chem. Eng. J. 324 (2017) 336–346.
[24] A.A. Rownaghi, F. Rezaei, M. Stante, J. Hedlund, Selective dehydration of methanol to dimethyl ether on ZSM-5 nanocrystals, Appl. Catal. B: Environ. 119–120 (2012) 56–61.
[25] S. Chen, X. Chang, G. Sun, T. Zhang, Y. Xu, Y. Wang, C. Pei, J. Gong, Propane dehydrogenation: catalyst development, new chemistry, and emerging technologies, Chem. Soc. Rev. 50 (2021) 3315–3354.
[26] F. Jiang, et al., Propane dehydrogenation over Pt/TiO2-Al2O3 Catalysts. ACS, Catalysis 5 (2018) 438–447.
[27] P. Krawiec, P.L. De Cola, R. Gläser, J. Weitkamp, C. Weidenthaler, S. Kaskel, Oxide foams for the synthesis of high-surface-area vanadium nitride catalysts, Adv. Mater. 18 (2006) 505–508.
[28] Q. Shen, H. Wei, L. Wang, Y. Zhou, Y. Zhao, Z. Zhang, D. Wang, G. Xu, D. Xu, Crystallization and aggregation behaviors of calcium carbonate in the presence of poly (vinylpyrrolidone) and sodium dodecyl sulfate, J. Phys. Chem. B 109 (2005) 18342–18347.
[29] M. Petráš, B. Wichterlová, High-temperature interaction of vanadium pentoxide with H-ZSM-5 zeolite. ESR and IR study, J. Phys. Chem. 96 (1992) 1805–1809.
[30] D.P. Debecker, K. Bouchmella, R. Delaigle, P. Eloy, C. Poleunis, P. Bertrand, E. M. Gaigneaux, P.H. Mutin, One-step non-hydrolytic sol – gel preparation of efficient V2O5 -TiO2 catalysts for VOC total oxidation, Appl. Catal. B: Environ. 94 (2010) 38–45.
[31] G. Silversmit, D. Depla, H. Poelman, G.B. Marin, R.De Gryse, An XPS study on the surface reduction of V2O5 (001) induced by Ar+ ion bombardment, Surf. Sci. 600 (2006) 3512–3517.
[32] B.R. Tak, S. Dewan, A. Goyal, R. Pathak, V. Gupta, A.K. Kapoor, S. Nagarajan, R. Singh, Point defects induced work function modulation of β-Ga2O3, Appl. Surf. Sci. 465 (2019) 973–978.
[33] W. Ren, Z. Ai, F. Jia, L. Zhang, Low temperature preparation and visible light photocatalytic activity of mesoporous carbon-doped crystalline TiO2, Appl. Catal. B: Environ. 69 (2007) 138–144.
[34] W. Yang, X. Yang, J. Jia, C. Hou, H. Gao, Y. Mao, C. Wang, J. Lin, X. Luo, Oxygen vacancies confined in ultrathin nickel oxide nanosheets for enhanced electrocatalytic methanol oxidation, Appl. Catal. B: Environ. 244 (2019) 1096–1102.
[35] H. Mori, C. Wen, J. Otomo, K. Eguchi, H. Takahashi, Investigation of the interaction between NiO and yttria-stabilized zirconia (YSZ) in the NiO/YSZ composite by temperature-programmed reduction technique, Appl. Catal. A: Gen. 245 (2003) 79–85.
[36] T.A. Zepeda, B. Pawelec, A. Infantes-Molina, R.I. Yocupicio, G. Alonso-Núñez, S. Fuentes, J.N. Diaz de León, J.L.G. Fierro, Ortho-xylene hydroisomerization under pressure on HMS-Ti mesoporous silica decorated with Ga2O3 nanoparticles, Fuel 158 (2015) 405–415.
[37] M. Xu, S. He, H. Chen, G. Cui, L. Zheng, B. Wang, M. Wei, TiO 2 − x -modified ni nanocatalyst with tunable metal − support interaction for water − gas shift reaction, ACS Catal. 7 (2017) 7600–7609.
[38] P.B. Sanguineti, M.A. Baltanás, A.L. Bonivardi, Copper-gallia interaction in Cu-Ga2O3-ZrO2 catalysts for methanol production from carbon oxide(s) hydrogenation, Appl. Catal. A: Gen. 504 (2015) 476–481.
[39] V. Boosa, S. Varimalla, M. Dumpalapally, N. Gutta, V.K. Velisoju, N. Nama, V. Akula, Influence of Brønsted acid sites on chemoselective synthesis of pyrrolidones over H-ZSM-5 supported copper catalyst, Appl. Catal. B: Environ. 292 (2021), 120177.
[40] E. Nowicka, C. Reece, S.M. Althahban, K.M.H. Mohammed, S.A. Kondrat, D. J. Morgan, Q. He, D.J. Willock, S. Golunski, C.J. Kiely, G.J. Hutchings, Elucidating

the role of CO_2 in the soft oxidative dehydrogenation of propane over ceria-based catalysts, ACS Catal. 8 (2018) 3454–3468.
[41] T. Bauer, S. Maisel, D. Blaumeiser, J. Vecchietti, N. Taccardi, P. Wasserscheid, A. Bonivardi, A. Görling, J. Libuda, Operando DRIFTS and DFT study of propane dehydrogenation over solid- and liquid-supported GaxPty catalysts, ACS Catal. 9 (2019) 2842–2853.
[42] Z. Ren, Z. Wu, W. Song, W. Xiao, Y. Guo, J. Ding, S.L. Suib, P.X. Gao, Low temperature propane oxidation over Co3O4 based nano-array catalysts: Ni dopant effect, reaction mechanism and structural stability, Appl. Catal. B, Environ. 180 (2016) 150–160.
[43] Y. Wang, W. Zheng, F. Chen, X. Zhan, Mechanistic study of propylene oxidation over a Bi – molybdate catalyst by in situ DRIFTS and probe molecules, Appl. Catal. A: Gen. 351 (2008) 75–81.
[44] G. Li, N. Li, Y. Sun, Y. Qu, Z. Jiang, Z. Zhao, Z. Zhang, J. Cheng, Z. Hao, Effecient defect engineering in Co-Mn binary oxides for low-temperature propane oxidation, Appl. Catal. B: Environ. 282 (2021), 119512.
[45] A.H.S. Kootenaei, J. Towfighi, A. Khodadadi, Y. Mortazavi, Stability and catalytic performance of vanadia supported on nanostructured titania catalyst in oxidative dehydrogenation of propane, Applied Surface Science 298 (2014) 26–35.